ACCSCIENCE PUBLISHING

International Journal of Bioprinting

RESEARCH ARTICLE

Dual-nozzle 3D-printed calcium sulfate/polylactic acid scaffold incorporating linezolid microspheres for effective repair of femoral condyle defects in rats

Xiaojie Tang[1,2†], Chenxu Li[1†], Yanan Wang[3†], Hai Huang[2], Tongshuai Xu[2], Shannan Cao[2], Changlin Lv[1], Xiaofan Du[1], Shuqing Chen[1], Wenkang Yang[1], Jiale Shao[1], Yukun Du[1*], and Yongming Xi[1*]

[1]Department of Orthopaedic Surgery, Affiliated Hospital of Qingdao University, Qingdao, Shandong, China

[2]Yantai Affiliated Hospital of Binzhou Medical University, Yantai, Shandong, China

[3]Department of Nuclear Medicine, Xuzhou Central Hospital, Xuzhou, Jiangsu, China

[†]These authors contributed equally to this work.

***Corresponding authors:**
Yongming Xi
(xym700118@163.com)

Yukun Du
(qdfydyk0728@163.com)

Citation: Tang X, Li C, Wang Y, *et al*. Dual-nozzle 3D-printed calcium sulfate/polylactic acid scaffold incorporating linezolid microspheres for effective repair of femoral condyle defects in rats. *Int J Bioprint*. 2025;11(5):333-349. doi: 10.36922/IJB025270069

Received: July 4, 2025
1st revised: August 4, 2025
2nd revised: August 18, 2025
Accepted: August 25, 2025
Published online: August 27, 2025

Abstract

Large, complex bone defects pose a significant clinical challenge. Conventional bone grafting approaches cannot simultaneously achieve tissue regeneration and infection prevention, resulting in impaired healing outcomes and prolonged treatment cycles. Existing therapeutic strategies lack integrated solutions capable of concurrently providing infection prevention and osteogenesis promotion within a single platform. This study developed a novel multifunctional composite scaffold using dual-nozzle three-dimensional printing technology to simultaneously achieve infection prevention and accelerated bone regeneration. Linezolid-loaded polylactic-co-glycolic acid microspheres (LMS) were uniformly dispersed within the pores of calcium sulfate/polylactic acid (CS/PLA) scaffolds to successfully construct the composite scaffold. *In vitro* characterization revealed uniform distribution of microspheres within the scaffold pores, with the fabricated CS/PLA-LMS demonstrating excellent biocompatibility and mechanical properties, achieving an elastic modulus of 87 MPa. Furthermore, the composite scaffold effectively inhibited *Staphylococcus aureus* activity *in vitro*. *In vivo* rat femoral condyle defect model revealed that the composite scaffold significantly enhanced bone formation compared to blank controls. Additionally, bone volume fraction increased by 3.2 times, and trabecular spacing decreased by 50%, with mechanistic analysis indicating activation of the phosphoinositide 3-kinase-protein kinase B signaling pathway. The integrated design successfully prevented infection-related complications while promoting robust osteogenesis, offering a clinically relevant solution for treating complex bone defects where infection prevention and regenerative capacity are primary therapeutic concerns.

Keywords: Bone defect repair, Dual-nozzle three-dimensional printing, Calcium sulfate, Linezolid microspheres

1. Introduction

Bone defect refers to the loss or damage of bone tissue caused by trauma, infection, tumor resection, or other etiologies, representing a common clinical issue in orthopedics.[1] The repair and regeneration of bone defects constitute a complex biological process. Although bone tissue possesses intrinsic self-healing capacity, this natural mechanism often proves insufficient in cases of extensive or critical-sized defects, necessitating the use of bone grafts to facilitate regeneration.[2,3] Over two million bone grafting procedures are performed globally each year, making it the second most common type of tissue transplantation after blood transfusion.[4,5] While autologous and allogeneic bone grafts are considered the gold standard for bone defect repair,[4–6] these materials have certain limitations.[7] Autologous bone grafts yield good results but may cause complications, pain, increased blood loss, and limited availability of graft material.[8,9] Allogeneic bone grafts avoid issues related to the donor site but may face challenges such as immune rejection or poor biocompatibility.[10–12] Furthermore, infection poses a significant challenge in the treatment of bone defects.[13] Bacteria can proliferate at the defect site, releasing toxins and inflammatory mediators that damage bone tissue and blood vessels, hindering regeneration.[5,10] Infected bone defects are also prone to a range of complications, including chronic osteomyelitis, bone necrosis, and arthritis.[14] These complications not only complicate treatment but may also lead to permanent functional impairment and disability. Therefore, effectively preventing and controlling infection to accelerate the repair of bone defects is crucial in clinical practice.[15,16]

Emerging materials and technologies for bone defect repair exhibit significant developmental potential.[17] Three-dimensional (3D) printing technology utilizes bioinks and customized implants to create complex, personalized bone substitutes.[18–20] Among these, fused deposition modeling is the most common technique, enabling precise control over the internal porosity, pore size, and interconnected structure of biomaterials.[21] Polylactic acid (PLA), a medical polymer synthesized from lactic acid, features a stable chemical structure, excellent plasticity, and mechanical properties.[22] Additionally, PLA can undergo controlled degradation without producing toxic byproducts.[23,24] The United States Food and Drug Administration approved its biomedical applications in the 1970s, and it remains widely used in this field.[25] Calcium sulfate (CS), tricalcium phosphate, and hydroxyapatite are typical bone-filling materials.[26] Among them, CS is widely used clinically as a filling support material for compressive fractures due to its good tolerance, excellent absorbability, and dual role in inhibiting fibrous tissue proliferation while promoting bone regeneration.[27–29] Furthermore, polylactic-co-glycolic acid (PLGA) microspheres demonstrate numerous advantages in drug delivery for bone repair. Firstly, they enable efficient drug delivery, ensuring effective concentrations at the lesion site and significantly enhancing therapeutic outcomes. Secondly, PLGA microspheres can function as sustained-release systems, precisely controlling the drug release rate, prolonging the biological activity of the drug in the body, and reducing the frequency of administration.[30–32] Additionally, PLGA microspheres exhibit excellent biocompatibility and biodegradability.

The current study developed a 3D-printed CS/PLA composite scaffold incorporating linezolid (LN)-loaded microspheres (LMS), which combines the properties of infection prevention and bone defect repair. Initially, PLGA copolymer microspheres containing LN were prepared to achieve controlled and sustained drug release. Then, utilizing dual-nozzle 3D printing technology, a porous CS/PLA scaffold was created, which enabled consistent LMS integration within the scaffold pores. A comprehensive evaluation was conducted on the composite scaffold's structural morphology, mechanical properties, *in vitro* drug release profile, and antibacterial activity. Finally, transcriptomic analyses alongside *in vitro* and *in vivo* experiments demonstrated the scaffold's superior osteogenic capabilities, mediated via the phosphoinositide 3-kinase (PI3K)-protein kinase B (Akt) signaling pathway. This engineered bone material not only surpasses natural cancellous bone in mechanical performance but also demonstrates outstanding biocompatibility, minimizing the risk of immune rejection. Furthermore, incorporating LMS into the material enables sustained and stable drug release to surrounding tissues, effectively preventing and controlling infections, thus accelerating bone tissue regeneration and repair (Figure 1). The development of this multifunctional material provides a novel method and means to treat bone defects and prevent implant infection, potentially improving patients' speed of recovery and quality of life.

2. Materials and methods

2.1. Materials

Linezolid was purchased from Beijing Epson Technology Co., Ltd. (China). Phosphate-buffered saline (PBS), minimum essential medium alpha (α-MEM), trypsin-ethylenediaminetetraacetic acid solution, and cell counting kit-8 (CCK-8) were obtained from Gibco (America). Fetal

bovine serum (FBS) was sourced from Wisent (China). PLGA was acquired from Shanghai Yuanye Bio-Technology Co., Ltd., China, while polyvinyl alcohol was purchased from Acros Organics (Belgium). Dichloromethane (DCM) was purchased from Sinopharm Group (China), and PLA was purchased from Acmec Biochemical Co., Ltd. (China). Sodium alginate (SA) and CS were obtained from Aladdin Industrial Corporation (China).

2.2. Preparation of linezolid-loaded microspheres

This study employed the solvent evaporation method of double emulsion (W/O/W) to prepare drug microspheres. A certain amount of LN was dissolved in 1 mL of purified water to form the internal aqueous phase. A defined amount of PLGA was dissolved in 9 mL of DCM, and 200 μL of 1% Tween-80 was added and mixed to form the oil phase. The internal aqueous phase was then added dropwise into the oil phase, followed by emulsification using an ultrasonic cell disruptor (Ningbo Scientz Biotechnology Co., Ltd, China) under an ice bath for 10 min (200 W, 7 s on/3 s off), resulting in a stable milky primary emulsion. This primary emulsion was then slowly and evenly introduced into 40 mL of polyvinyl alcohol solution (external aqueous phase) under continuous stirring for 4 h to allow complete evaporation of DCM. The resulting double emulsion was left to stand for an hour until the microspheres had fully precipitated. The microspheres were then transferred to centrifuge tubes, washed twice with distilled water, and centrifuged twice. After pre-freezing at −80°C for 4 h, the microspheres were freeze-dried under vacuum for 12 h to obtain the final LMS.[33]

2.3. Characterization of linezolid-loaded microspheres

The Marvel 3000 particle size analyzer from Malvern Instruments (United Kingdom) was used to measure the microspheres' particle sizes. Moreover, a scanning electron microscope (EVO/LS15, Carl Zeiss, Germany) was used to examine the micro-morphology of the microspheres.

2.4. Construction of linezolid standard curve

Using an electronic balance, 25 mg of LN was measured and dissolved in 50 mL of PBS buffer solution. This solution was transferred to a 50 mL volumetric flask to prepare a stock solution of 0.5 mg/mL LN. A dilution concentration of 200, 100, 50, 25, 12.5, 6.25, and 3.125 μg/mL was then obtained by diluting 4, 2, 1, 0.5, 0.25, 0.125, and 0.0625 mL of the stock solution with 10 mL of PBS. The optical density (OD) values at 280 nm for each concentration were measured using a ultraviolet spectrophotometer (Beijing Purkinje General Instrument Co., Ltd. China), and a standard curve of LN in PBS buffer was generated.

2.5. *In vitro* release test of linezolid-loaded microspheres

To evaluate the *in vitro* release profile of LN, 100 mg of LMS and 100 mg of standard LN were suspended in 50 mL of PBS and incubated in a constant-temperature shaker (Changzhou Runhua Electric Appliances Co., Ltd. China) at 37°C and 100 rpm. Each day, 4 mL of the solution was sampled for analysis, and an equal volume of fresh PBS was added to maintain consistent conditions. The absorbance at 280 nm was recorded using a spectrophotometer, and the mean values were employed to calculate the daily and cumulative drug release amounts, as well as the sustained release rate.

2.6. *In vitro* antibacterial test of linezolid-loaded microspheres

The model bacterium used in the antibacterial test was *Staphylococcus aureus* (*S. aureus* [ATCC 25923] courtesy from Binzhou Medical University Affiliated Yantai Hospital). The strain was inoculated into an appropriate volume of sterile liquid medium and cultured overnight at 37°C to prepare a bacterial suspension. The prepared suspension (1.54×10^8 CFU/mL) was spread onto sterile Muller–Hinton agar plates (Jinan Babio Biotechnology Co., Ltd., China). Prior to the antibacterial test, LMS was exposed to ultraviolet light for 10 min to ensure sterilization. LMS was then added to the medium and incubated at 37°C for 24 h. The diameter of the inhibition zone was measured and recorded to determine the degree of bacterial inhibition. In addition, we also tested the antibacterial activity of LMS at Days 3, 7, and 14.

2.7. Preparation of sodium alginate hydrogel carrier

A 2% SA hydrogel was selected as the carrier. Two grams of SA powder were weighed and dissolved in 100 mL of 1% dilute hydrochloric acid solution. The SA powder was stirred continuously at a uniform speed for 8 h until completely dissolved, resulting in a uniform gel-like solution. The SA hydrogel was then prepared.

2.8. Design and preparation of composite scaffolds

A computer-aided design software was used to design the printing model of the CS/PLA scaffold. A dual-nozzle 3D printer was employed to fabricate a scaffold structure with dimensions of $3.5 \times 2.5 \times 0.3$ cm^3, a line width of 300 μm, and a pore size of 500 μm, with adjacent layers printed at a 90° orientation. The mixing ratio of CS powder and PLA powder was based on previous studies, where the powders were blended at a mass ratio of 1:9 before being fed into the hot-melt nozzle.[33] The printing temperature was set between 110 and 130°C, with a printing speed of 12 mm/s. A total of 0.6 g of microspheres was dispersed in 10 mL of

1% SA hydrogel containing 400 μL of Tween-80. The resulting mixture was loaded into a room-temperature nozzle and printed at a speed of 12 mm/s. After printing, the scaffold was placed in a refrigerator (4°C) to dry for 8 h. The control group was printed using only the hot-melt nozzle without including drug-loaded microspheres. The printed scaffold was precisely cut using a 4 mm diameter specialized punch to prepare circular scaffolds with a diameter of 4 mm and a thickness of 3 mm for subsequent use.

2.9. Scanning electron microscopy and energy-dispersive X-ray spectroscopy characterization

The CS/PLA and CS/PLA-LMS scaffolds' overall look and microstructural features were analyzed through scanning electron microscopy (SEM). Elemental analysis of the CS/PLA and CS/PLA-LMS scaffolds was conducted using energy-dispersive X-ray spectroscopy (EDS; Carl Zeiss AG Merlin, Germany) to examine the distribution of elements within the scaffolds.

2.10. Determination of mechanical properties of stent

A universal testing machine (Instron, America) was used to conduct compression tests on three CS/PLA blank scaffolds and three drug-loaded CS/PLA composite scaffolds, with the compression speed set to 5 mm/min. The experimental data from each sample were analyzed to record the maximum stress strength, and stress–strain curves were plotted for both scaffold groups. The elastic modulus and compressive strength for each scaffold group were assessed by finding the slope of the secant line between two points in the 10%–20% strain range.

2.11. Preparation of two groups of scaffold material extracts

Scaffold materials from each group were sliced into 5 × 5 mm^2 squares and sterilized using hydrogen peroxide. The extraction medium, physiological saline, was added at a ratio of 6 cm^2/mL according to the surface area of the samples. To produce scaffold extracts, the scaffolds were incubated at 37°C for 24 h and then stored at 4°C for future use.

2.12. Cell culture

Bone marrow stromal cells (BMSCs) were extracted from 2-week-old Sprague–Dawley rats (n = 3). After cervical dislocation, the tibia and femur were isolated, with the ends of both bones trimmed. The bone marrow cavity was flushed with a syringe, and the suspension was homogenized and cultured in a medium containing 10% FBS, 100 U/mL penicillin, and 100 μg/mL streptomycin at 37°C with 5% carbon dioxide. The culture medium was refreshed every 2 days. BMSCs were utilized for subsequent experiments within five passages. To create the osteogenic differentiation medium, 10 mM glycerol phosphate, 50 μL ascorbic acid, and 100 nM dexamethasone were added to the α-MEM culture medium.

2.13. *In vitro* cytotoxicity and cell proliferation assays of the two groups of scaffold materials

The cytotoxicity and cell proliferation of the scaffold materials were assessed using fluorescein isothiocyanate-phalloidin staining and the CCK-8 assay. An initial density of 25,000 BMSCs per well was seeded in a 24-well plate and incubated overnight at 37°C. The supernatant was then removed, and osteogenic induction medium, with or without 50% extract, was added to the wells. Once the cell confluence reached 70–80%, the cells were washed twice with PBS for 10 min each. They were then fixed with 4% paraformaldehyde for 20 min and washed twice with PBS. Fluorescein isothiocyanate-phalloidin at 5 μg/mL was added for staining at room temperature for 30–60 min, followed by two PBS washes. 4',6-diamidino-2-phenylindole was used to stain the nuclei for 10 min, and the cells were washed twice with PBS again. Excess moisture was removed, and a fluorescence mounting medium was added for observation under a confocal microscope (Leica, America).

After being initially planted at a density of 5000 cells per well in a 96-well plate, the BMSCs were incubated overnight at 37°C. The supernatant was then removed, and osteogenic induction medium, with or without 50% extract, was added to the plate for incubation at 24, 48, and 72 h. After incubation, the supernatant was replaced with 100 μL of serum-free medium containing 10% CCK-8 reagent. Following a 2-h incubation at 37°C, the OD values of each group were measured using a microplate reader, and a bar graph was plotted based on the OD values. Cell viability (%) can be calculated with the formula in **Equation (I)**:

$$\text{Cell viability (\%)} = \frac{OD(\textit{experimental group}) - OD(\textit{blank group})}{OD(\textit{negative control group}) - OD(\textit{blank group})} \times 100\% \quad \text{(I)}$$

2.14. Evaluation of the *in vitro* antibacterial properties of the two scaffold material groups

Using a pre-prepared bacterial suspension (1.54 × 10^8 CFU/mL), bacteria were spread onto sterile Muller–Hinton agar plates. Prior to the antimicrobial test, both groups of scaffolds were exposed to ultraviolet light for 10 min to complete the sterilization process. The scaffolds

were then placed in the medium and incubated at 37°C for 24 h. The extent of bacterial inhibition was determined by measuring and recording the diameter of the inhibition zones. In addition, we also tested the antibacterial activity of CS/PLA-LMS at Days 3, 7, and 14.

2.15. *In vitro* osteogenic potential of the two groups of scaffolds

The influence of scaffolds on the osteogenic differentiation potential of BMSCs was measured with an alkaline phosphatase (ALP) staining kit (P0321S, Beyotime, China). In a 12-well plate, BMSCs were seeded, divided into the blank group, CS/PLA group, and CS/PLA-LMS group, at a density of 1×10^5 cells per well. Following cell adhesion, particular treatments were given to each group, and they were maintained in osteogenic induction medium for 7 days. ALP staining was then performed using the kit, with p-nitrophenyl phosphate serving as the substrate to assess ALP activity in the samples. ALP activity was quantified by assessing the absorbance at 405 nm using the ALP assay kit.

To evaluate the impact of scaffolds on the degree of mineralization of BMSCs, the extracted BMSCs were seeded at a density of 1×10^5 cells per well onto a 12-well plate under the same grouping (blank, CS/PLA, and CS/PLA-LMS). Following cell adhesion, the cells received the designated treatments before being cultivated for 21 days in osteogenic induction medium. Subsequently, the cells were rinsed twice with PBS, fixed with 4% paraformaldehyde for 15 min, and then washed three times with PBS again. They were then stained with Alizarin Red solution (Cyagen Biosciences, China) for 30 min at room temperature. The mineralization level of BMSCs was quantitatively assessed by dissolving the bound Alizarin Red in a 10% cetylpyridinium chloride (Sigma-Aldrich, USA) solution for an hour. The OD of the resulting solution was then measured at 570 nm using a spectrophotometer.

The BMSCs from the designated groups were seeded into a 6-well plate at a density of 2×10^5 cells per well. Following the application of specific treatments, the cells were cultured in osteogenic induction medium for 7 days. The gene expression levels of osteogenic differentiation markers, including Runt-related transcription factor 2 (*Runx2*), osteocalcin (*Ocn*), *Alp*, and collagen I (*Col1a1*), were analyzed using quantitative polymerase chain reaction (qPCR). Total RNA was extracted using Trizol reagent, and then reverse-transcribed into complementary DNA with the PrimeScript RT reagent kit (TaKaRa Biotechnology [Dalian] Co., Ltd. Japan). Gene expression was measured using real-time qPCR (Applied biosystems, America) with SYBR Green Master Mix (Yeasen Biotechnology (Shanghai) Co., Ltd. China). Primer sequences are shown in Table S1, Supporting Information.

Total protein was extracted from BMSCs by lysis in radioimmunoprecipitation assay buffer for protein blot analysis following the same treatments and a 14-day culture period (with non-induced BMSCs serving as the sham group, induced but untreated BMSCs as the control group, and other groups treated with different scaffold extracts). Protein concentration was determined using the bicinchoninic acid protein assay kit (Shanghai Biyuntian Biological Co., Ltd., China). Proteins were then mixed with loading buffer, boiled, and subjected to sodium dodecyl sulfate-polyacrylamide gel electrophoresis before being transferred to a polyvinylidene fluoride membrane. The membrane was blocked for an hour using non-fat milk, followed by the addition of primary antibodies against RUNX2 (1:1000), OCN (1:1000), ALP (1:1000), and *Col1a1* (1:500), and incubated overnight at 4°C. It was then treated with secondary antibodies conjugated with horseradish peroxidase. Protein bands were visualized using an enhanced chemiluminescence kit, and Scion imaging software (version 4.0) captured the images. ImageJ software (version 1.46) was used for quantitative analysis. All antibodies, including the secondary antibodies (goat anti-mouse IgG and goat anti-rabbit IgG), were obtained from Abcam. Transcriptome sequencing was also performed to observe the underlying osteogenic mechanisms.

2.16. Transcriptome sequencing analysis

After 2 weeks of culture, mRNA was extracted from bone-induced BMSC cells treated with CS/PLA-LMS extraction solution using Trizol reagent. Bone-induced BMSC cells without CS/PLA-LMS extraction solution served as the control. RNA sequencing was conducted at Shanghai Berhao Biotechnology Co., Ltd. (China) to determine the mRNA expression profiles across different groups. mRNAs with a $\log_2$ fold change ($\log_2$FC) of ≥1 or ≤−1 and a q-value ≤ 0.05 were considered differentially expressed. To depict the number of differentially expressed mRNAs, a volcano plot was constructed, featuring both upregulated and downregulated transcripts. The gene expression trend was visualized using a heatmap. Gene Ontology (GO) and Kyoto Encyclopedia of Genes and Genomes (KEGG) analyses were performed to identify the enriched signaling pathways of differentially expressed genes. A scatter bubble plot was used to display the top 30 significantly enriched signaling pathways with a p-value of less than 0.05.

2.17. Animal model and surgical procedures

A femoral bone defect model was established in 8-week-old male Sprague–Dawley rats. All animals were acclimated at a supervised animal facility for at least 2 weeks before trials began, during which time their health was monitored every day. Three sets of four rats each were randomly assigned: CS/PLA, CS/PLA-LMS, and control (untreated defect).

The rat femoral condyle defect model was established according to the method reported in the literature.[34,35] Specifically, after shaving the rat's fur and disinfecting with povidone-iodine, a longitudinal incision was made on the lateral side of the patellar ligament to expose the lateral femoral condyle. A 4 mm orthopedic drill was used to create a bone defect with a diameter of 4 mm and a depth of 3 mm. The defect area was then irrigated with saline solution to remove bone debris. Subsequently, scaffolds from different groups were placed into the hole. Finally, the surgical site was washed, sutured, and disinfected. The three groups were the following: the blank control group, the CS/PLA group, and the CS/PLA-LMS group.

At 4- and 8-week postoperative intervals, the animals were euthanized through cervical dislocation. The entire femora were collected by removing the surrounding soft tissues, and major organs such as the heart, liver, spleen, lungs, and kidneys were collected for biosafety assessment. All samples were then fixed with 4% paraformaldehyde.

2.18. Micro-computed tomography evaluation

After fixation, the femoral specimens were scanned using micro-computed tomography (CT; Bruker Skyscan, Belgium). Subsequently, bone volume fraction (BV/TV), trabecular thickness, trabecular number, and trabecular separation were calculated using DataViewer (version 1.5.6.2) and the Comprehensive TeX Archive Network software (version 1.20.8.0). Three-dimensional reconstruction of the femur was performed with CTVox (version 3.3.0).

2.19. Histological analysis and immunofluorescence staining

Following fixation and decalcification, specimens were embedded in paraffin, sectioned into 4 μm slices, and mounted on glass slides. For histological evaluation, sections were stained with hematoxylin and eosin (H&E) and Masson's trichrome to assess tissue morphology and bone regeneration.

For immunofluorescence staining, sections were permeabilized with 0.1% Triton X-100, blocked with 5% bovine serum albumin, and incubated overnight at 4°C with primary antibodies targeting *Col1a1*, OSN, and RUNX2. After washing, sections were incubated with Alexa Fluor 488-conjugated secondary antibodies, and nuclei were counterstained with 4',6-diamidino-2-phenylindole. Fluorescent images were acquired using a digital slide scanner (KFBIO, China) and analyzed quantitatively with ImageJ software (version 1.46).

2.20. Statistical analysis

The statistical program Statistical Package for Social Sciences version 24 was used to analyze the data. All samples were measured in triplicate, unless otherwise indicated, and the findings are shown as mean ± standard deviation. The least significant difference test was used for multiple group comparisons for normally distributed data in the context of a one-way analysis of variance. The threshold for statistical significance was set at $p < 0.05$. GraphPad Prism version 10 was used to construct data-related figures.

3. Results

3.1. Characterization of linezolid-loaded microspheres

The microspheres prepared in this study appeared as a white, fine sandy powder, evenly dispersed and free of clumping (Figure 1A). SEM showed that the microspheres exhibited a regular spherical structure (Figure 1B and C). Particle size analysis of the LMS powder indicated a normal distribution of particle sizes (Figure 1D). The Dv (90) of the LMS sample was measured at 46.2 μm, signifying that 90% of the microspheres had a diameter smaller than 46.2 μm, thereby meeting the anticipated size specifications. The equation for the LN standard curve was determined to be (**Equation II;** Figure 1E):

$$y = 27.568x + 10.176, R^2 = 0.999 \quad \text{(II)}$$

3.2. Sustained release and antibacterial effects of linezolid-loaded microspheres

The drug release curve of LMS over 20 days is illustrated in Figure 1F and G. During the first 3 days, the residual drugs were still present on the microspheres, which led to a sudden release. From Day 4 onward, the residual drugs on the microspheres were completely released, and the drug concentration at this stage was solely attributable to microsphere degradation. A significant release was observed starting from Day 11. By Day 20, the cumulative drug release rate reached 87.53 ± 1.79%. In terms of the clinical application of LN, a consensus among Chinese experts indicates that the trough concentration of LN should be maintained above 2.0 μg/mL to prevent the development of resistance. In this study, LMS exhibited a relatively stable drug release rate starting from Day 4, with an average daily release of approximately 4.8 ± 0.419 μg/mL for 100 mg of microspheres in 50 mL of PBS solution, surpassing the minimum trough concentration recommended for treating complex infections. Furthermore, *in vitro* antibacterial assays demonstrated that 10 mg of LMS (Figure 1H) showed significant antibacterial activity against *S. aureus* ATCC-29213 in agar culture, with an inhibition zone diameter of about 35.33 ± 0.057 mm within 24 h, compared to the blank control microspheres lacking LMS. Notably, the LMS maintained

effective antibacterial activity for up to 14 days (Figure S1A, Supporting Information).

3.3. Preparation and characterization of calcium sulfate/polylactic acid-linezolid-loaded microsphere scaffolds

In this study, the white rectangular solid CS/PLA scaffold was created according to the printing method in Figure S2, Supporting Information. The printing volume was 3.5 × 2.5 × 0.3 cm^3 (Figure 2A). SEM images show a homogeneous distribution of pore diameters with a line width of about 300 μm and pore sizes of around 500 μm (Figure 2E–H). White particles are uniformly distributed within the pores of the CS/PLA-LMS scaffold (Figure 2C). Electron microscopy observations show that multiple microspheres are evenly distributed on the scaffold's surface and internal pores, interconnected by SA hydrogel to prevent them from dislodging (Figure 2I–L). The stress–strain curves for both material groups are presented in Figure 2B and D. The elastic modulus of the CS/PLA scaffold was measured at 67.537 ± 2.867 MPa, while the CS/PLA-LMS scaffold group showed an elastic modulus of 87.563 ± 3.256 MPa. Furthermore, EDS analysis revealed the elemental distribution within the CS/PLA scaffold (Figure 2M).

3.4. *In vitro* biocompatibility and antibacterial ability of calcium sulfate/polylactic acid-linezolid-loaded microsphere scaffolds

This study assessed the cytotoxic effects of scaffold extracts on BMSCs. Both phalloidin-cytoskeleton staining and CCK-8 assays demonstrated that the extracts from both scaffolds were non-toxic to the cells (Figures S3 and S4,

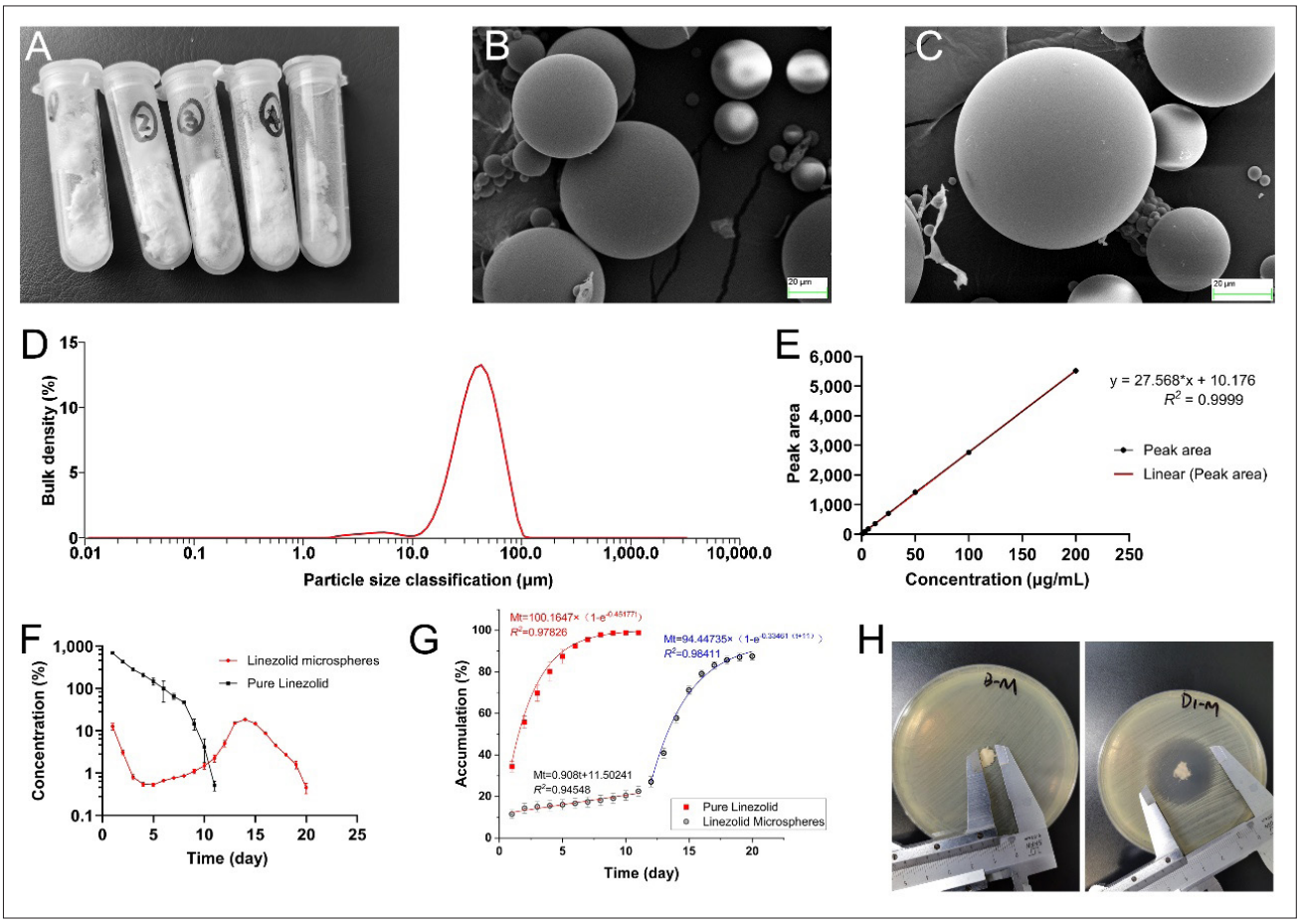

Figure 1. The physical properties and antibacterial capabilities of LMS. (A) Digital photographs of LMS, showing their spherical morphology and uniform size distribution. (B and C) Scanning electron microscopy images of LMS at different magnifications, highlighting their surface structure and texture. Scale bar: 20 μm. (D) Particle size distribution of LMS, indicating the size range and uniformity of the particles. (E) Linezolid (LN) standard curve, used to determine the drug concentration in release studies, demonstrating a linear relationship between concentration and absorbance. (F) Daily *in vitro* release efficiency of LMS, showing the release profile of LN over time under physiological conditions. (G) Cumulative *in vitro* release efficiency of LMS, illustrating the total drug release over a period of time, and demonstrating sustained release characteristics. (H) Antimicrobial properties of LMS *in vitro*, assessed by their ability to inhibit bacterial growth, with a comparison to control groups to highlight their efficacy. Abbreviation: LMS, linezolid-loaded microspheres.

Supporting Information). Additionally, the results of the cell adhesion assay on the composite scaffold demonstrated that cells adhered well to the scaffold surface, showing no significant difference compared to the blank scaffold (Figure 2N and O). We assessed the *in vitro* antibacterial properties of the two scaffold groups. With an inhibition zone diameter of roughly 20.97 ± 0.061 mm after 24 h, the CS/PLA-LMS scaffold demonstrated a noticeably better antibacterial activity against *S. aureus* ATCC-29213 in agar medium compared to the CS/PLA scaffold (Figure 2P). Furthermore, it maintained effective antibacterial activity for up to 14 days (Figure S5B, Supporting Information).

3.5. *In vitro* osteogenesis of calcium sulfate/polylactic acid-linezolid-loaded microsphere scaffolds

On Day 7 of osteogenic induction, BMSCs co-cultured with scaffold extracts were subjected to ALP staining and quantitative analysis to evaluate their osteogenic differentiation potential (Figure 3A and B). The results demonstrated that while both the CS/PLA and CS/PLA-LMS scaffold groups exhibited higher staining intensity compared to the control group, no statistically significant difference was observed between the two scaffold groups. To further investigate mineralization characteristics,

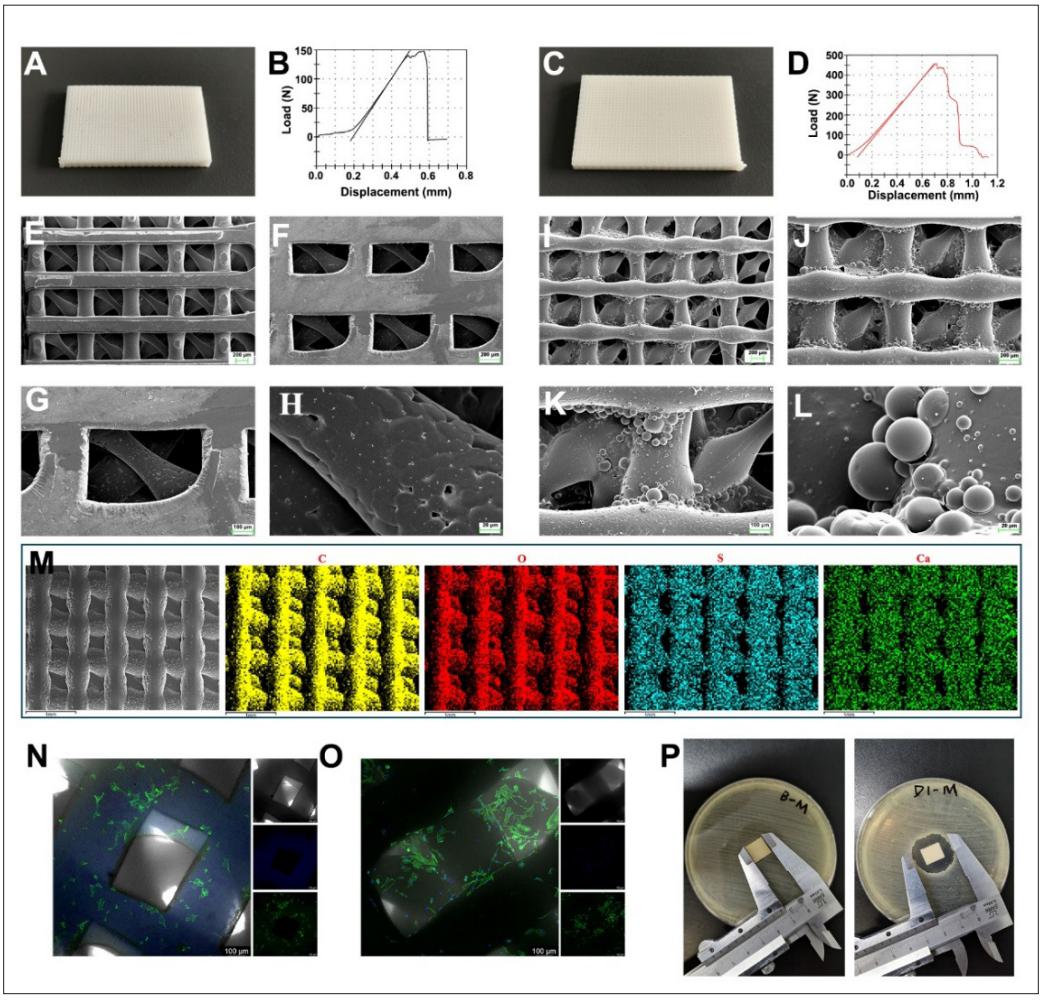

Figure 2. The physical properties and *in vitro* antibacterial capabilities of the composite scaffolds. (A and C) Digital photographs of the CS/PLA and CS/PLA-LMS scaffolds, showing their overall structure, with LMS incorporated into the composite scaffold. (B and D) Compressive stress–strain curves for the CS/PLA and CS/PLA-LMS scaffolds, illustrating their mechanical properties; the CS/PLA-LMS scaffold exhibits higher load-bearing capacity. (E–H) SEM images of the CS/PLA scaffold at various magnifications, showing its porous structure and surface features. Scale bars: 20, 100, and 200 μm; (I–L) SEM images of the CS/PLA-LMS composite scaffold, highlighting the integration of LMS within the matrix. Scale bars: 20, 100, and 200 μm; (M) Elemental mapping images showing the distribution of carbon (C), oxygen (O), sulfur (S), and calcium (Ca) elements, confirming LMS incorporation. Scale bar: 1 mm; (N and O) Cell adhesion experiments performed in the blank scaffold and composite scaffold groups proved that composite scaffolds have good cell adhesion ability. Scale bar: 100 μm. (P) *In vitro* antibacterial test showing greater inhibition zones around the CS/PLA-LMS scaffold compared to CS/PLA. Abbreviations: CS, calcium sulfate; LMS, linezolid-loaded microsphere; PLA, polylactic acid; SEM, scanning electron microscopy.

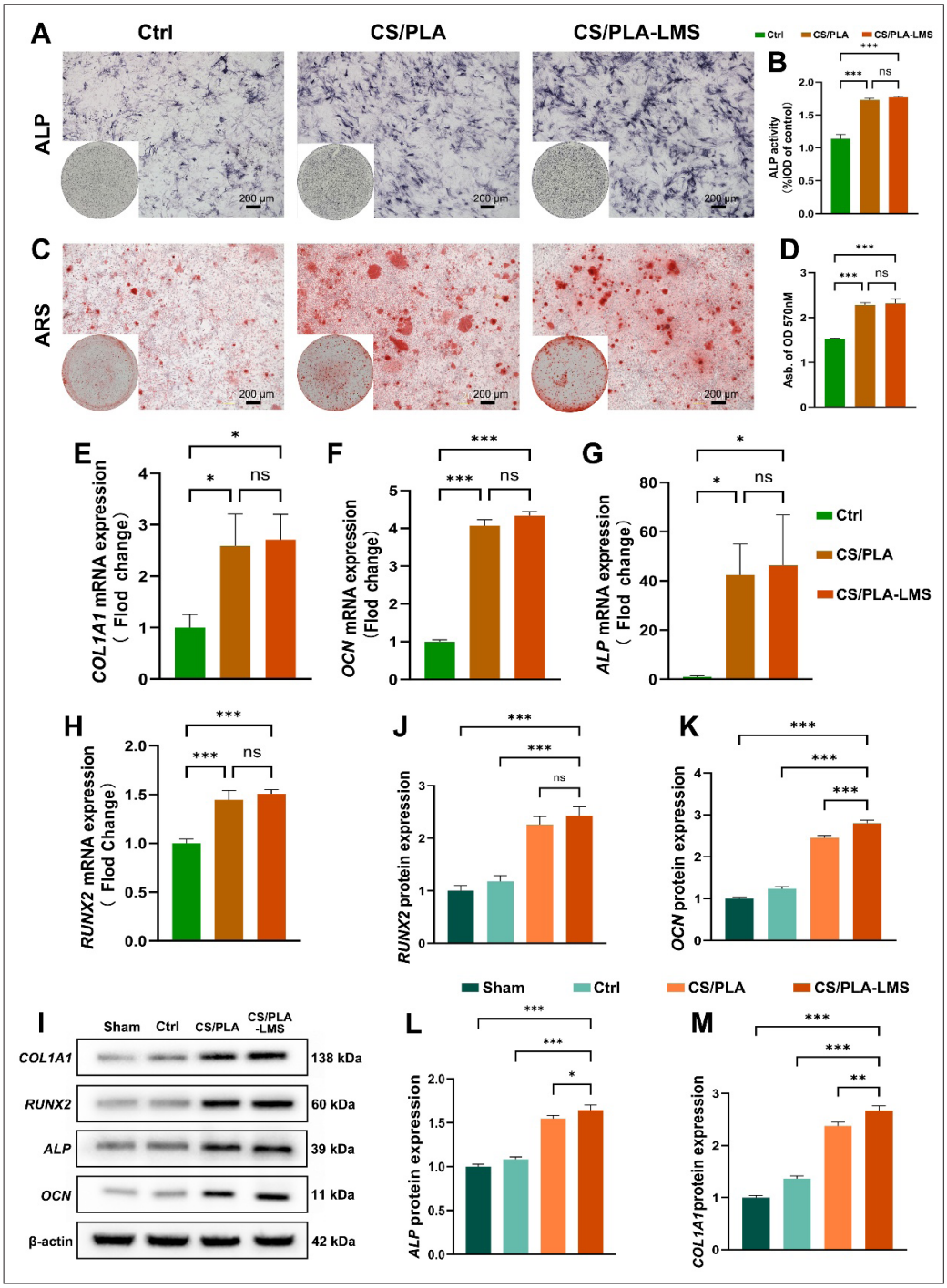

Figure 3. The osteogenic capability of BMSCs co-cultured with various scaffolds *in vitro*. (A) Microscopic images and macroscopic observations of ALP staining in BMSCs after 7 days of culture with different scaffold extracts. Scale bar: 200 μm. (B) Quantification of ALP activity, showing the osteogenic activity in the composite scaffold group. (C) Microscopic images and macroscopic observations of Alizarin Red (ARS) staining in BMSCs after 21 days of osteogenic induction, visualizing mineralization. Scale bar: 200 μm. (D) Quantification of ARS staining, indicating the degree of mineralization. (E–H) Gene expression analysis of osteogenic markers in BMSCs co-cultured with scaffold extracts, including *Col1a1* (E), *Ocn* (F), *Alp* (G), and *Runx2* (H). The composite scaffold group upregulates the expression of osteogenic genes. (I–M) Protein expression levels of BMSCs cultured in different scaffold extracts: RUNX2 (J), OCN (K), ALP (L), and *Col1a1* (M). Significant differences in protein expression were observed, with enhanced expression in the CS/PLA and CS/PLA-LMS group. All statistical data are represented as mean ± standard deviation ($n = 3$; *$p < 0.05$; **$p < 0.01$; ***$p < 0.001$). Abbreviations: ALP, alkaline phosphatase; BMSC, bone marrow stromal cell; COL1A1: Collagen type 1; CS, calcium sulfate; Ctrl, Control; LMS, linezolid-loaded microsphere; ns, non-significant; OCN, osteocalcin; OD, optical density; PLA, polylactic acid; RUNX2, runt-related transcription factor 2.

Alizarin Red S staining was subsequently performed on BMSCs co-cultured with scaffold extracts (Figure 3C and D). After 21 days of culture, both scaffold groups showed a significant increase in calcium nodule formation relative to the control group. qPCR analysis demonstrated that, compared to the control group, the expression levels of osteogenesis-related genes (*Runx2*, *Ocn*, *Alp*, and *Col1a1*) were upregulated in BMSCs co-cultured with the two scaffold extract groups (Figure 3E–H). Western blot analysis revealed that the expression levels of osteogenic proteins (RUNX2, OCN, ALP, and *Col1a1*) were significantly elevated in both scaffold groups compared to the control and uninduced (Sham) groups (Figure 3I–M). These results suggest that the CS/PLA-LMS scaffold has strong osteogenic-promoting properties.

3.6. Osteogenesis mechanism of calcium sulfate/polylactic acid-linezolid-loaded microsphere scaffold

Building on the results of previous experiments, we conducted mRNA sequencing on BMSCs from different treatment groups to further investigate the potential mechanisms by which CS/PLA-LMS promotes bone formation. Principal component analysis and differential gene clustering demonstrated a clear distinction between the two sample groups (Figure 4A and C). In total, 4118 differential genes were identified, with 181 genes upregulated and 250 genes downregulated (Figure 4B). GO functional enrichment analysis was performed based on the expression of these differential genes. The differential genes were significantly enriched in the cytoplasm, reaction to stimulus, developmental processes, and catalytic activity, as seen in Figure 4D. Additionally, KEGG pathway analysis revealed a notable enrichment of differential genes in the PI3K-Akt signaling pathway and protein processing in the endoplasmic reticulum (Figure 4E).

To validate this mechanism, we examined the expression and phosphorylation levels of key PI3K/Akt pathway proteins (PI3K and Akt) in the blank group (non-osteogenic induction), control group, CS/PLA group, and CS/PLA-LMS group using western blot. The CS/PLA and CS/PLA-LMS groups showed higher phosphorylation levels of PI3K and Akt than the control and blank groups, according to both western blot and quantitative data (Figure 4F–H). This activation effect was significantly reduced after the treatment of CS/PLA and CS/PLA-LMS groups with the specific PI3K inhibitor LY294002 (Figure 4I and J). Subsequent experiments revealed that LY294002 treatment significantly downregulated the expression levels of key osteogenic markers (*Col1a1*, RUNX2, ALP, and OCN) compared to other groups (Figure 4K–O), with levels markedly lower than the control group. These findings confirm that CS/PLA-LMS enhances osteogenic activity through the PI3K-Akt signaling pathway.

3.7. *In vivo* evaluation of calcium sulfate/polylactic acid-linezolid-loaded microsphere scaffolds

This study evaluated the therapeutic effect of composite stents by establishing a femoral condyle defect model (Figure S5, Supporting Information). Micro-CT reconstruction and quantitative analysis revealed that the CS/PLA-LMS scaffold group exhibited remarkable temporal advantages in bone defect repair (Figure 5A and B). At 4 weeks post-implantation, the BV/TV in the CS/PLA-LMS group reached 63.12%, representing a 3.2-fold increase compared to the control group (19.79%) and significantly exceeding the CS/PLA group (48.29%). The trabecular thickness (165.98 μm) in the CS/PLA-LMS group achieved 97.6% of normal bone levels (~170 μm), while the trabecular spacing (141.16 μm) demonstrated a 50.1% reduction relative to the control group (282.49 μm), indicating early formation of dense osseous structures.

By 8 weeks post-operation, the CS/PLA-LMS group displayed advanced regenerative characteristics: BV/TV further increased to 63.30%. Trabecular thickness (133.14 μm) and trabecular number (0.0048 mm^{-1}) exhibited 21.3% and 25.1% increases compared to the 4-week timepoint, respectively. Dynamic comparison demonstrated that the CS/PLA-LMS group maintained a stable weekly bone formation rate (ΔBV/TV: 0.04%), surpassing the control group (0.004%).

Neo-bone development and maturation were confirmed by histological evaluation using Masson's trichrome staining and H&E. At 4 weeks post-implantation, minimal osseous regeneration was observed in the control group, with defect regions predominantly occupied by marrow cells (Figure 5C). In contrast, scaffold pores in both CS/PLA and CS/PLA-LMS groups were infiltrated with fibrous tissue, accompanied by newly formed osseous tissue surrounding the fibrous matrices. By 8 weeks, fibrous components in experimental groups were replaced by organized bone tissue, while the control group exhibited persistent soft tissue infiltration. Masson's trichrome staining revealed more mature collagen organization in the CS/PLA-LMS group, demonstrating intense blue staining characteristic of mature bone (Figure 5D), consistent with the micro-CT findings.

Immunofluorescence staining of osteogenic-related proteins (*Col1a1*, OCN, and RUNX2) was performed on tissues harvested at 4 and 8 weeks postoperatively (Figure 6A and B). Compared to the control group, both the CS/PLA and CS/PLA-LMS groups showed a marked increase in the expression levels of these proteins.

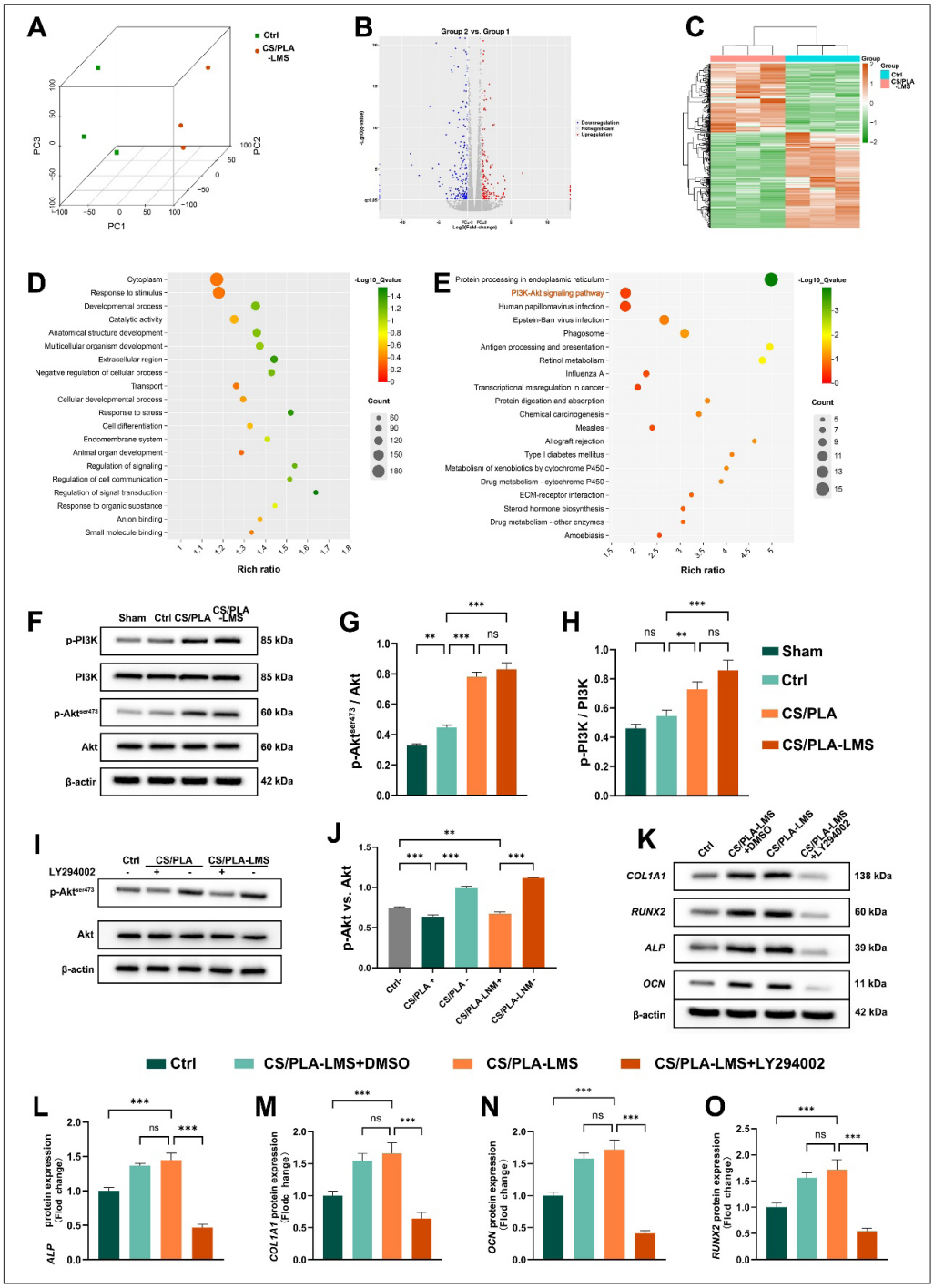

Figure 4. The CS/PLA-LMS scaffold promotes osteogenesis through the PI3K/Akt signaling pathway. (A) Principal component (PC) analysis showing the distribution of different groups. (B) Volcano plot illustrating differentially expressed genes between the groups. (C) Heatmap representing the differential gene expression patterns among the groups. (D) Gene ontology (GO) enrichment analysis of differentially expressed genes, highlighting the key biological processes involved. (E) KEGG pathway enrichment analysis, showing the most significantly enriched pathways in the different groups. (F–H) Western blot analysis of the phosphorylation levels of PI3K-Akt in BMSCs cultured with CS/PLA-LMS extracts. (I and J) Inhibition of the PI3K-Akt pathway using LY294002 and its effect on phosphorylation levels. (K–O) Expression levels of osteogenic-related proteins: ALP (L), *Col1a1* (M), OCN (N), and RUNX2 (O) after PI3K-Akt pathway inhibition. All statistical data are represented as mean ± standard deviation ($n = 3$; $^{*}p < 0.05$; $^{**}p < 0.01$; $^{***}p < 0.001$). Abbreviations: Akt, protein kinase B; ALP, alkaline phosphatase; BMSC, bone marrow stromal cell; COL1A1, Collagen type 1; CS, calcium sulfate; Ctrl, Control; DMSO, dimethyl sulfoxide; KEGG: Kyoto Encyclopedia of Genes and Genomes; LMS, linezolid-loaded microsphere; ns, non-significant; OCN, osteocalcin; PI3K, phosphoinositide 3-kinase; PLA, polylactic acid; RUNX2, runt-related transcription factor 2.

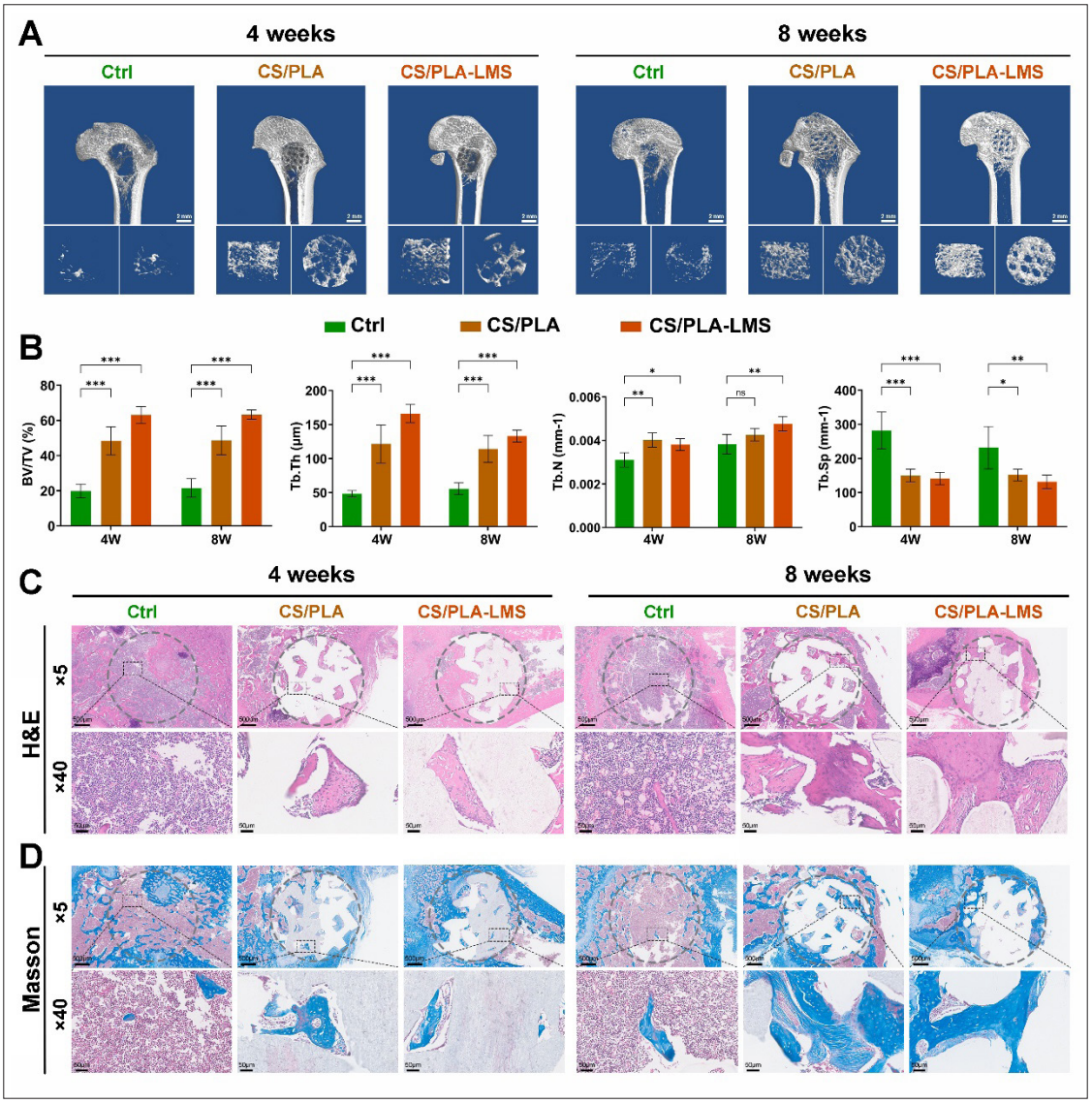

Figure 5. Evaluation of osteogenic capability at 4- and 8-weeks post-scaffold implantation. (A) Three-dimensional reconstructed micro-CT images of bone defects treated with different scaffolds at 4 and 8 weeks, showing the progression of bone healing. Scale bar: 2 mm (B) Quantitative analysis of micro-CT results, including bone volume/total volume (BV/TV), trabecular thickness (Tb.Th), trabecular number (Tb.N), and trabecular separation (Tb.Sp) at both 4 and 8 weeks. (C) Hematoxylin and eosin (H&E) staining of bone tissue sections at 4 and 8 weeks, showing tissue morphology and bone regeneration. Scale bars: 500 μm and 50 μm; magnifications: 5× and 40×. (D) Masson's trichrome staining of bone tissue sections at 4 and 8 weeks, visualizing collagen deposition and bone matrix formation. Scale bars: 500 and 50 μm; magnifications: 5× and 40×. All statistical data are represented as mean ± standard deviation ($n = 4$; $^{*}p < 0.05$; $^{**}p < 0.01$; $^{***}p < 0.001$). Abbreviations: CS, calcium sulfate; CT, computed tomography; Ctrl: control; LMS, linezolid-loaded microsphere; ns, non-significant; PLA, polylactic acid.

These findings validate the critical role of the composite scaffold in promoting bone regeneration through two synergistic mechanisms. First, the scaffold provides mechanical support and a porous microenvironment, which synergistically establishes an optimal osteogenic niche for bone repair. Secondly, as a drug delivery system, microspheres can release LN continuously, thus achieving the effect of long-term prevention of infection.

Additionally, H&E staining was performed on the animals' internal organs (heart, liver, spleen, lung, and kidney) (Figure S6, Supporting Information). No obvious pathological changes, such as inflammatory infiltration,

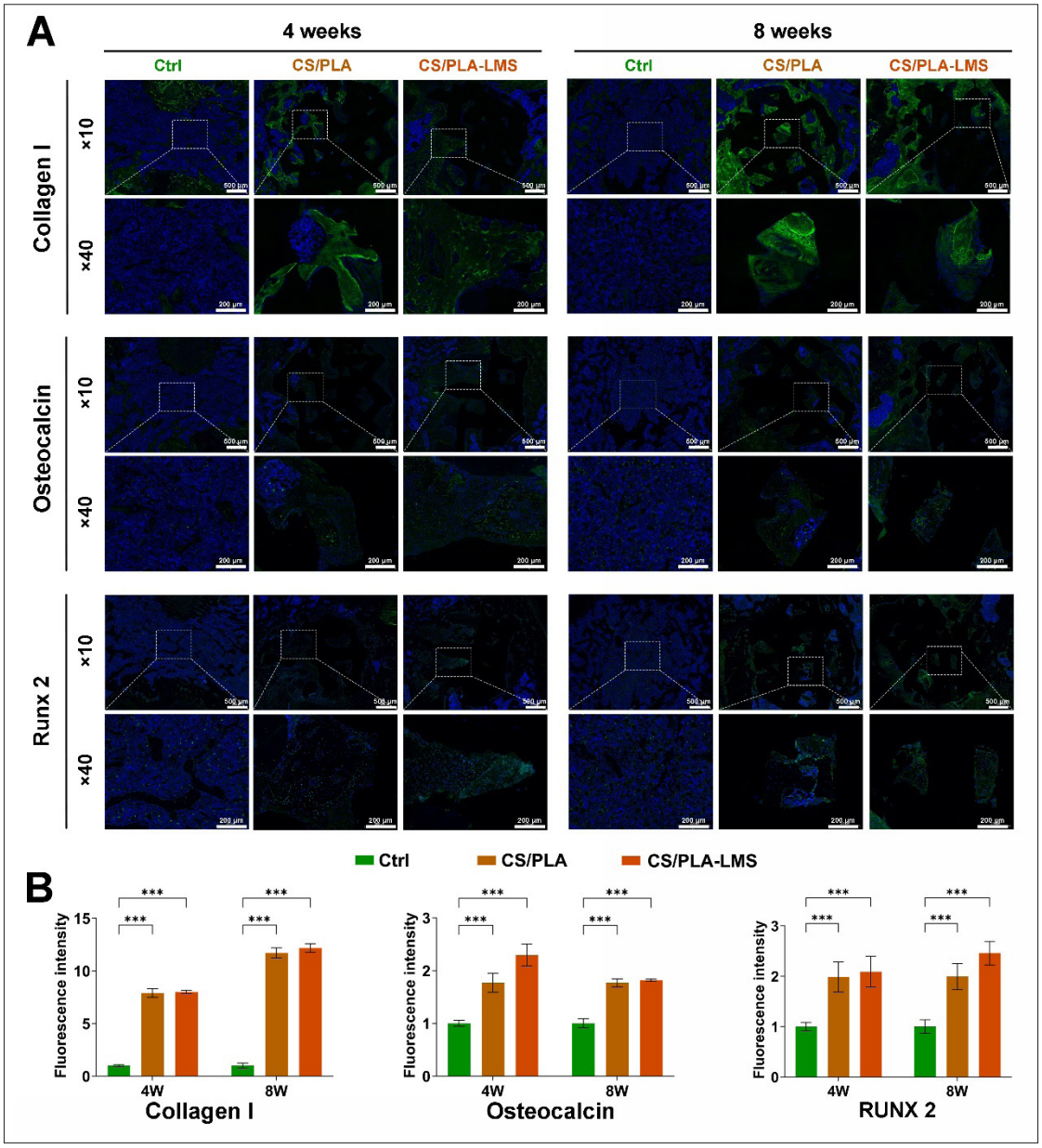

Figure 6. Immunofluorescence staining analysis of osteogenic activity. (A) Immunofluorescence staining for collagen I, osteocalcin, and RUNX2 at 4- and 8-weeks post-implantation, showing expression in bone tissue. Scale bars: 200 and 500 μm; magnifications: 10× and 40×. (B) Quantitative analysis of the fluorescence intensity for collagen I, osteocalcin, and RUNX2 at 4 and 8 weeks, indicating the osteogenic activity in the different scaffold groups. All statistical data are represented as mean ± standard deviation ($n = 4$; $^{*}p < 0.05$; $^{**}p < 0.01$; $^{***}p < 0.001$). Abbreviations: CS, calcium sulfate; Ctrl, control; LMS, linezolid-loaded microsphere; ns, non-significant; PLA, polylactic acid; RUNX2, runt-related transcription factor 2.

apoptosis, or necrosis, were observed in any groups, demonstrating the safety of the scaffold.

4. Discussion

In this study, we successfully developed a multifunctional composite scaffold (CS/PLA-LMS) using dual-nozzle 3D printing technology, which combined infection prevention and enhanced osteogenesis. The scaffold, incorporating LMS, demonstrated significant improvements in both antibacterial properties and bone regeneration. The results indicated that the scaffold effectively supported bone repair in a rat femoral condyle defect model while simultaneously preventing infection.

Research on carrier materials and preparation techniques for drug-loaded sustained-release microsphere systems provides innovative strategies for treating chronic

diseases, including infections and cancer.[36] In this study, the PLGA microsphere material, a commonly used polymeric carrier, was employed due to its biodegradability and non-toxicity in humans.[37] Additionally, the European Medicines Agency and the United States Food and Drug Administration have approved PLGA, citing its superior safety, degradability, and biocompatibility. These attributes make PLGA highly suitable for applications in biomedical engineering and drug delivery systems.[38,39] Yuan *et al.*[40] achieved controlled release of magnesium ions to promote bone regeneration by co-embedding magnesium oxide and magnesium carbonate in PLGA microspheres.[40] Moreover, Hickey *et al.*[41] developed a novel dexamethasone/PLGA microsphere system that provides immediate release of dexamethasone and sustained release for over a month, suitable for continuous delivery of anti-inflammatory drugs in implantable medical devices.[41]

Three-dimensional-printed scaffolds are viewed as ideal clinical bone substitute materials due to their controllable internal structures featuring pores that support cell survival and metabolism, facilitating nutrient exchange and accelerating osteogenesis.[42] In this experiment, the chosen scaffold materials are PLA and CS. PLA is highly biocompatible, produces biodegradable byproducts (such as lactic acid) that the body can metabolize and eliminate, and degrades at controlled rates, making it widely employed in the production of bone biomaterials.[43] To heal major bone lesions, Wang *et al.*[44] used fused deposition modeling-3D printing technology to create PLA/nano β-tricalcium phosphate composite scaffolds for bone tissue engineering.[44] Similarly, Senatov *et al.*[45] integrated bone morphogenetic protein-2 and erythropoietin into PLA scaffolds to develop recombinant protein scaffolds for bone defect repair. Additionally, CS, an inorganic component of bone, enhances scaffold biocompatibility, mechanical strength, and hydrophilicity. The incorporation of CS facilitates bone cell differentiation and proliferation, promoting calcium and phosphate mineral deposition within the scaffold and thereby accelerating new bone formation.[46] Liu *et al.*[47] further highlighted the effectiveness of α-CS hemihydrate/nano-hydroxyapatite composites loaded with metformin in promoting bone regeneration in a rat cranial defect model. A key advantage of this experiment is the utilization of computer-aided design to create the scaffold's internal structure. Compared to traditional immersion methods, the dual-nozzle 3D printing technology enables precise and uniform distribution of drug carrier microspheres within the scaffold's pores, thus addressing the issue of uneven distribution.[48] Uneven distribution could result in insufficient residual drug microspheres as the scaffold degrades, potentially failing to achieve effective antibacterial concentrations.

In large complex bone defects, perioperative infection constitutes a pivotal determinant of surgical outcome. Drug release kinetics revealed sustained release from the microsphere system over 20 days, with cumulative drug release reaching 87.53 ± 1.79%, demonstrating the capacity for extended antimicrobial protection. The sustained release profile corresponds with established clinical guidelines advocating LN trough levels exceeding 2.0 μg/mL to mitigate resistance emergence. Critically, the microsphere-mediated drug release consistently surpassed minimum therapeutic thresholds, ensuring robust infection prophylaxis.[49]

Despite the elastic modulus of this scaffold (87 MPa) being slightly higher than the 2–12 MPa range of human cancellous bone,[50] it remains significantly lower than that of clinically prevalent titanium metal implants.[51] Stress shielding occurs when the implant absorbs most mechanical loads, thereby reducing the load borne by surrounding bone tissue, which may inhibit bone remodeling and regeneration.[52] While the scaffold can provide short-term support for bone defect areas, future research should further optimize its mechanical properties to better match the elastic modulus of natural bone, thereby achieving biomechanical compatibility with native bone tissue.

Our findings also show that the CS/PLA-LMS scaffold activates the PI3K-Akt signaling pathway, which plays a key role in osteoblast differentiation and bone formation.[53] *In vitro* experiments showed that the CS/PLA-LMS scaffold significantly upregulated osteogenic markers such as RUNX2, OCN, ALP, and *Col1a1*. *In vivo* results further confirmed this mechanism.

Histological and micro-CT evaluations showed significant improvements in bone regeneration. In the *in vivo* rat model, the CS/PLA-LMS scaffold group exhibited a 3.2-fold increase in BV/TV and a 50% reduction in trabecular spacing compared to the control group. Histological analysis revealed well-organized bone tissue in the scaffold-treated groups, indicating accelerated bone healing. These observations are consistent with the osteogenic capabilities of the scaffold. Although the CS/PLA-LMS scaffold group demonstrated superior osteogenesis-related parameters in both radiographic and histopathological analyses compared to the CS/PLA group, no statistically significant difference was observed between the two groups. We hypothesized that this phenomenon may be associated with subclinical infection: while some animals showed no overt infection symptoms, low-virulence bacterial colonization might still exist. Such "occult infections" could compromise bone healing quality. The CS/PLA-LMS scaffold creates a more favorable

microenvironment for bone regeneration by preventing and controlling these subclinical infections.

5. Conclusion

In conclusion, we engineered a new CS/PLA-LMS scaffold with a unique porous architecture that enhances cell growth, metabolism, and proliferation within its pores, and assists in the treatment of pathological bone defects. The LMS has characteristics of sustained release. Using dual-nozzle 3D printing technology, these microspheres were uniformly distributed within the pores of the CS/PLA scaffold and released the drug gradually as the scaffold degraded. The osteogenic properties of CS/PLA-LMS were realized through the activation of the PI3K/Akt signaling pathway, and the inhibition of this pathway markedly reduced the osteogenic capacity of CS/PLA-LMS. Furthermore, tests on animals and *in vitro* cells demonstrated that the composite scaffold has outstanding biomechanical performance, compatibility, and degradability without cytotoxic effects, successfully facilitating osteogenesis and the restoration of bone defect areas. The creation of more effective multifunctional biomimetic scaffolds to address the therapeutic needs of complicated complex bone defects is anticipated with the help of additional optimization of the CS/PLA-LMS scaffold to improve its mechanical strength and prevent infection.

Acknowledgments

None.

Funding

This study was supported by the Taishan Scholar Project of Shandong Province, China (No.tstp 20250511).

Conflict of interest

The authors declare that they have no conflict of interest.

Author contributions

Conceptualization: Hai Huang, Tongshuai Xu
Data curation: Jiale Shao
Formal analysis: Jiale Shao
Funding acquisition: Yongming Xi
Investigation: Shannan Cao, Changlin Lv
Methodology: Shuqing Chen, Wenkang Yang
Resources: Shannan Cao, Changlin Lv
Supervision: Yongming Xi
Visualization: Xiaofan Du
Writing–original draft: Xiaojie Tang, Chenxu Li, Yanan Wang
Writing–review & editing: Yukun Du, Yongming Xi

Ethics approval

All animal-related experiments in this study adhered to the guidelines for the care and use of laboratory animals set forth by the National Institutes of Health (NIH). The experimental animals were provided by the Yantai Campus of Binzhou Medical University. All animal experiments were approved by the Animal Experimentation Committee of Yantai Campus, Binzhou Medical University (Animal Research Approval No.: 2024-L066).

Consent for publication

Not applicable.

Availability of data

Data will be made available upon request to the corresponding author.

References

1. Jihan M, Qi B, Bayaniahangar R, *et al*. Nanomaterials for bone tissue regeneration: updates and future perspectives. *Nanomedicine (Lond)*. 2019;14(22):2987-3006.
doi: 10.2217/nnm-2018-0445

2. Spicer PP, Kretlow JD, Young S, Jansen JA, Kasper FK, Mikos AG. Evaluation of bone regeneration using the rat critical size calvarial defect. *Nat Protoc*. 2012;7(10): 1918-1929.
doi: 10.1038/nprot.2012.113

3. Gugala Z, Gogolewski S. Regeneration of segmental diaphyseal defects in sheep tibiae using resorbable polymeric membranes: a preliminary study. *J Orthop Trauma*. 1999;13(3):187-195.
doi: 10.1097/00005131-199903000-00006

4. Dimitriou R, Jones E, McGonagle D, Giannoudis PV. Bone regeneration: current concepts and future directions. *BMC Med*. 2011;9:66.
doi: 10.1186/1741-7015-9-66

5. Campana V, Milano G, Pagano E, *et al*. Bone substitutes in orthopaedic surgery: from basic science to clinical practice. *J Mater Sci Mater Med*. 2014;25(10):2445-2461.
doi: 10.1007/s10856-014-5240-2

6. Roberts TT, Rosenbaum AJ. Bone grafts, bone substitutes and orthobiologics: the bridge between basic science and clinical advancements in fracture healing. *Organogenesis*. 2012;8(4):114-124.
doi: 10.4161/org.23306

7. Nazeer MA, Onder OC, Sevgili I, Yilgor E, Kavakli IH, Yilgor I. 3D printed poly (lactic acid) scaffolds modified with chitosan and hydroxyapatite for bone repair applications. *Mater Today Commun*. 2020;25:101515.
doi: 10.1016/j.mtcomm.2020.101515

8. Khan SN, Cammisa FP Jr, Sandhu HS, Diwan AD, Girardi FP, Lane JM. The biology of bone grafting. *J Am Acad Orthop Surg*. 2005;13(1):77-86.
doi: 10.5435/00124635-200501000-00009

9. Chiarello E, Cadossi M, Tedesco G, *et al*. Autograft, allograft and bone substitutes in reconstructive orthopedic surgery. *Aging Clin Exp Res*. 2013;25(Suppl 1):S101-S103.
doi: 10.1007/s40520-013-0088-8

10. Stevenson S, Horowitz M. The response to bone allografts. *J Bone Joint Surg Am*. 1992;74(6):939-950.
doi: 10.2106/00004623-199274060-00009

11. Stevenson S. The immune response to osteochondral allografts in dogs. *J Bone Joint Surg Am*. 1987;69(4):573-582.

12. Stevenson S, Li XQ, Martin B. The fate of cancellous and cortical bone after transplantation of fresh and frozen tissue-antigen-matched and mismatched osteochondral allografts in dogs. *J Bone Joint Surg Am*. 1991;73(8):1143-1156.

13. Kavanagh N, Ryan EJ, Widaa A, *et al*. Staphylococcal osteomyelitis: disease progression, treatment challenges, and future directions. *Clin Microbiol Rev*. 2018;31(2): e00084-17.
doi: 10.1128/CMR.00084-17

14. Yıldırım A, Kapukaya A, Mertsoy Y, Yiğit Ş, Çaçan MA, Atiç R. Management of open fractures using a noncontact locking plate as an internal fixator. *Indian J Orthop*. 2017;51(3):312-317.
doi: 10.4103/0019-5413.205686

15. Masters EA, Ricciardi BF, Bentley KLdM, Moriarty TF, Schwarz EM, Muthukrishnan G. Skeletal infections: microbial pathogenesis, immunity and clinical management. *Nat Rev Microbiol*. 2022;20(7):385-400.
doi: 10.1038/s41579-022-00686-0

16. Vallet-Regí M, Lozano D, González B, Izquierdo-Barba I. Biomaterials against bone infection. *Adv Healthc Mater*. 2020;9(6):e1901647.
doi: 10.1002/adhm.201901647

17. Prince GE, Yang X, Fu J, *et al*. Yolk-porous shell biphasic bioceramic granules enhancing bone regeneration and repair beyond homogenous hybrid. *Mater Sci Eng C Mater Biol Appl*. 2019;100:433-444.
doi: 10.1016/j.msec.2019.03.026

18. Yang Y, Chu L, Yang S, *et al*. Dual-functional 3D-printed composite scaffold for inhibiting bacterial infection and promoting bone regeneration in infected bone defect models. *Acta Biomater*. 2018;79:265-275.
doi: 10.1016/j.actbio.2018.08.015

19. Zhang L, Yang G, Johnson BN, Jia X. Three-dimensional (3D) printed scaffold and material selection for bone repair. *Acta Biomater*. 2019;84:16-33.
doi: 10.1016/j.actbio.2018.11.039

20. Liu W, Li J, Cheng M, *et al*. A surface-engineered polyetheretherketone biomaterial implant with direct and immunoregulatory antibacterial activity against methicillin-resistant Staphylococcus aureus. *Biomaterials*. 2019;208:8-20.
doi: 10.1016/j.biomaterials.2019.04.008

21. El-Rashidy AA, Roether JA, Harhaus L, Kneser U, Boccaccini AR. Regenerating bone with bioactive glass scaffolds: a review of in vivo studies in bone defect models. *Acta Biomater*. 2017;62:1-28.
doi: 10.1016/j.actbio.2017.08.030

22. Lopes MS, Jardini A, Maciel Filho R. Poly (lactic acid) production for tissue engineering applications. *Procedia Eng*. 2012;42:1402-1413.

23. Maadani AM, Salahinejad E. Performance comparison of PLA- and PLGA-coated porous bioceramic scaffolds: mechanical, biodegradability, bioactivity, delivery and biocompatibility assessments. *J Control Release*. 2022;351:1-7.
doi: 10.1016/j.jconrel.2022.09.022

24. Ma B, Han J, Zhang S, *et al*. Hydroxyapatite nanobelt/polylactic acid Janus membrane with osteoinduction/barrier dual functions for precise bone defect repair. *Acta Biomater*. 2018;71:108-117.
doi: 10.1016/j.actbio.2018.02.033

25. Tyler B, Gullotti D, Mangraviti A, Utsuki T, Brem H. Polylactic acid (PLA) controlled delivery carriers for biomedical applications. *Adv Drug Deliv Rev*. 2016;107:163-175.
doi: 10.1016/j.addr.2016.06.018

26. Zwingenberger S, Nich C, Valladares RD, Yao Z, Stiehler M, Goodman SB. Recommendations and considerations for the use of biologics in orthopedic surgery. *BioDrugs*. 2012;26(4):245-256.
doi: 10.2165/11631680-000000000-00000

27. Kumar RA, Sivashanmugam A, Deepthi S, Bumgardner JD, Nair SV, Jayakumar R. Nano-fibrin stabilized CaSO4 crystals incorporated injectable chitin composite hydrogel for enhanced angiogenesis & osteogenesis. *Carbohydrate Polym*. 2016;140:144-153.
doi: 10.1016/j.carbpol.2015.12.077

28. Zhou Z, Buchanan F, Mitchell C, Dunne N. Printability of calcium phosphate: calcium sulfate powders for the application of tissue engineered bone scaffolds using the 3D printing technique. *Mater Sci Eng C Mater Biol Appl*. 2014;38:1-10.
doi: 10.1016/j.msec.2014.01.033

29. Aquino-Martínez R, Angelo AP, Pujol FV. Calcium-containing scaffolds induce bone regeneration by regulating mesenchymal stem cell differentiation and migration. *Stem Cell Res Ther*. 2017;8(1):265.
doi: 10.1186/s13287-017-0713-0

30. Mitragotri S, Burke PA, Langer R. Overcoming the challenges in administering biopharmaceuticals: formulation and delivery strategies. *Nat Rev Drug Discov*. 2014;13(9):655-672.

doi: 10.1038/nrd4363

31. Wright JC, Burgess DJ. *Long Acting Injections and Implants*. Springer Science & Business Media; 2011.

32. Jain R, Shah NH, Malick AW, Rhodes CT. Controlled drug delivery by biodegradable poly (ester) devices: different preparative approaches. *Drug Dev Ind Pharm*. 1998;24(8):703-727.
doi: 10.3109/03639049809047401

33. Li J, Li K, Du Y, *et al*. Dual-nozzle 3D printed nano-hydroxyapatite scaffold loaded with vancomycin sustained-release microspheres for enhancing bone regeneration. *Int J Nanomed*. 2023;18:307-322.
doi: 10.2147/ijn.S394366

34. Wang L, Wang J, Zhou X, *et al*. A new self-healing hydrogel containing hucMSC-derived exosomes promotes bone regeneration. *Front Bioeng Biotechnol*. 2020;8:564731.
doi: 10.3389/fbioe.2020.564731

35. Wang L, Wei X, He X, *et al*. Osteoinductive dental pulp stem cell-derived extracellular vesicle-loaded multifunctional hydrogel for bone regeneration. *ACS Nano*. 2024;18(12):8777-8797.
doi: 10.1021/acsnano.3c11542

36. Davidson BL, Hilfinger JM, Beer SJ. Extended release of adenovirus from polymer microspheres: potential use in gene therapy for brain tumors. *Adv Drug Deliv Rev*. 1997;27(1):59-66.

37. Rocha CV, Gonçalves V, da Silva MC, Bañobre-López M, Gallo J. PLGA-based composites for various biomedical applications. *Int J Mol Sci*. 2022;23(4):2034.
doi: 10.3390/ijms23042034

38. Wang Y, Qin B, Xia G, Choi SH. FDA's poly (lactic-co-glycolic acid) research program and regulatory outcomes. *AAPS J*. 2021;23(4):92.
doi: 10.1208/s12248-021-00611-y

39. Wan B, Bao Q, Burgess D. Long-acting PLGA microspheres: advances in excipient and product analysis toward improved product understanding. *Adv Drug Deliv Rev*. 2023;198:114857.
doi: 10.1016/j.addr.2023.114857

40. Yuan Z, Wei P, Huang Y, *et al*. Injectable PLGA microspheres with tunable magnesium ion release for promoting bone regeneration. *Acta Biomater*. 2019;85:294-309.
doi: 10.1016/j.actbio.2018.12.017

41. Hickey T, Kreutzer D, Burgess DJ, Moussy F. Dexamethasone/PLGA microspheres for continuous delivery of an anti-inflammatory drug for implantable medical devices. *Biomaterials*. 2002;23(7):1649-1656.
doi: 10.1016/s0142-9612(01)00291-5

42. Huiwen W, Shuai L, Jia X, *et al*. 3D-printed nanohydroxyapatite/methylacrylylated silk fibroin scaffold for repairing rat skull defects. *J Biol Eng*. 2024;18(1):22.
doi: 10.1186/s13036-024-00416-5

43. Sitthisang S, Hou X, Treetong A, *et al*. Nanomechanical mapping of PLA hydroxyapatite composite scaffolds links surface homogeneity to stem cell differentiation. *Sci Rep*. 2024;14(1):21097.
doi: 10.1038/s41598-024-72073-z

44. Wang W, Liu P, Zhang B, *et al*. Fused deposition modeling printed PLA/Nano β-TCP composite bone tissue engineering scaffolds for promoting osteogenic induction function. *Int J Nanomedicine*. 2023;18:5815-5830.
doi: 10.2147/ijn.S416098

45. Senatov F, Zimina A, Chubrik A, *et al*. Effect of recombinant BMP-2 and erythropoietin on osteogenic properties of biomimetic PLA/PCL/HA and PHB/HA scaffolds in critical-size cranial defects model. *Mater Sci Eng C Mater Biol Appl*. 2022;135:112680.
doi: 10.1016/j.msec.2022.112680

46. Gao S, Li J, Lei Q, *et al*. Calcium sulfate-Cu(2+) delivery system improves 3D-printed calcium silicate artificial bone to repair large bone defects. *Front Bioeng Biotechnol*. 2023;11:1224557.
doi: 10.3389/fbioe.2023.1224557

47. Liu S, Fu H, Lv Y, *et al*. α-Hemihydrate calcium sulfate/n-hydroxyapatite combined with metformin promotes osteogenesis in vitro and in vivo. *Front Bioeng Biotechnol*. 2022;10:899157.
doi: 10.3389/fbioe.2022.899157

48. Macedo J, Marques R, Vervaet C, Pinto JF. Production of bi-compartmental tablets by FDM 3D printing for the withdrawal of diazepam. *Pharmaceutics*. 2023;15(2):538.
doi: 10.3390/pharmaceutics15020538

49. Morata L, Cuesta M, Rojas JF, *et al*. Risk factors for a low linezolid trough plasma concentration in acute infections. *Antimicrob Agents Chemother*. 2013;57(4):1913-1917.
doi: 10.1128/aac.01694-12

50. Mandal S, Viraj, Nandi SK, Roy M. Effects of multiscale porosity and pore interconnectivity on in vitro and in vivo degradation and biocompatibility of Fe-Mn-Cu scaffolds. *J Mater Chem B*. 2021;9(21):4340-4354.
doi: 10.1039/d1tb00641j

51. Qin Y, Jing Z, Zou D, *et al*. A metamaterial scaffold beyond modulus limits: enhanced osteogenesis and angiogenesis of critical bone defects. *Nat Commun*. 2025;16(1):2180.
doi: 10.1038/s41467-025-57609-9

52. Wang Q, Chen Y, Ding H, *et al*. Optogenetic activation of mechanical nociceptions to enhance implant osseointegration. *Nat Commun*. 2025;16(1):3093.
doi: 10.1038/s41467-025-58336-x

53. Zhao SJ, Kong FQ, Jie J, *et al*. Macrophage MSR1 promotes BMSC osteogenic differentiation and M2-like polarization by activating PI3K/AKT/GSK3β/β-catenin pathway. *Theranostics*. 2020;10(1):17-35.
doi: 10.7150/thno.36930